



## Retinal vessel segmentation using a multi-scale medialness function

Elahe Moghimirad<sup>a</sup>, Seyed Hamid Rezatofghi<sup>a,b</sup>, Hamid Soltanian-Zadeh<sup>a,c,\*</sup>

<sup>a</sup> Control and Intelligent Processing Center of Excellence, School of Electrical and Computer Engineering, University of Tehran, Tehran 14395, Iran

<sup>b</sup> Research School of Information Sciences and Engineering (RSISE), College of Engineering and Computer Science, Australian National University, Canberra, ACT 0200, Australia

<sup>c</sup> Image Analysis Lab., Department of Radiology, Henry Ford Health System, Detroit, MI 48202, USA

### ARTICLE INFO

#### Article history:

Received 5 September 2010

Accepted 23 October 2011

#### Keywords:

Retinal vessel segmentation

Medialness function

Hessian matrix

Reconnection

Radius estimation

### ABSTRACT

Recently, automated segmentation of retinal vessels in optic fundus images has been an important focus of much research. In this paper, we propose a multi-scale method to segment retinal vessels based on a weighted two-dimensional (2D) medialness function. The results of the medialness function are first multiplied by the eigenvalues of the Hessian matrix. Next, centerlines of vessels are extracted using noise reduction and reconnection procedures. Finally, vessel radii are estimated and retinal vessels are segmented. The proposed method is evaluated and compared with several recent methods using images from the DRIVE and STARE databases.

© 2011 Elsevier Ltd. All rights reserved.

### 1. Introduction

Inspection of the optic fundus assists ophthalmologists in diagnosis and evaluation of general diseases, which include diabetes, hypertension, arteriosclerosis, cardiovascular diseases, stroke, and vascular/nonvascular retinal diseases like retinopathy of prematurity [1]. Initial symptoms of such diseases are revealed by morphological features of retinal veins and arteries such as diameter, length, branching angle, and tortuosity [2]. Thus, the measurement and recognition of the exact location of retinal blood vessels has diagnostic relevance for the ophthalmologists. However, because of the complex structure of vessels, manual tracking of retinal vessels is difficult. Furthermore, manual segmentation results vary a lot between inter- and intra-observers. Therefore, automated segmentation of retinal vessels in optic fundus images has been a subject of intensive research during recent years.

According to [3], automatic retinal segmentation methods generally fall into three categories: tracking, kernel-based, and classifier-based methods. In each category, several algorithms are proposed in [4–13]. In [4], a tracking method is presented, which is initialized by a generalized morphological order filter to determine approximate vessel centerlines, and uses a “Ribbon of Twins” (ROT) active contour model for segmenting and measuring retinal vessels. A novel multi-scale line tracking procedure is proposed by Vlachos and Dermatas [5]. In this method, an initial vessel network is obtained by map quantization of a multi-scale confidence matrix. The result is filtered by a median filter to

restore disconnected vessels and remove noisy structures. Finally, a post-processing step is applied to correct misclassified areas.

Several classifier-based methods are introduced in [6–10]. Soares et al. [6] suggest that feature vectors can be extracted from a two-dimensional Gabor wavelet transform and the pixel's intensity. Also, a Gaussian mixture model classifier can be used for classification. A method based on multi-scale feature extraction is introduced in [7] to automatically segment the retinal blood vessels from the background. The method uses the first and second derivatives of the image intensities in a multiple pass region growing algorithm. In another approach proposed by Ricci and Perfetti [8], two line operators are used to extract the feature vectors whilst a Linear Support Vector Machine (LSVM) is used as a classifier. In [9], a feature-based AdaBoost classifier (FABC) is applied for classifying 41-dimensional feature vectors constructed by encoding information from the local intensity structure, spatial properties, and geometry at multiple scales. Improved results are obtained in [10] where a 7-dimensional vector composed of gray-level and moment invariants-based features is calculated, and a neural network (NN) scheme is used for pixel classification.

The methods introduced by Mendonça and Campilho in [11], Yan Lam and Yan in [12], and Zhang et al. in [13] can be considered as kernel-based methods. In [11], Mendonça et al. segment retinal vessels using a combination of differential filters, that is difference of offset Gaussians filters (DoOG filters), to find vessel centerlines, along with an iterative region-growing method that integrates the contents of several binary images to fill the vessel segments. Yan Lam and Yan [12] suggest a scheme based on the Laplacian operator to segment blood vessels in the pathological retinal images. For this purpose, the centerlines of vessels are first detected using a normalized gradient vector field. Due to noise in pathological regions, noisy objects should be

\* Corresponding author. Tel.: +1 313 874 4482; fax: +1 313 874 4494.  
E-mail address: hamids@rad.hfh.edu (H. Soltanian-Zadeh).

eliminated from the image background. Therefore, at the next step, they are pruned based on centerline information. Zhang et al. [13] use an extension of the Matched Filter (MF) approach, named the MF-FDOG, which is a combination of the original matched filter and the first-order derivative of Gaussian (FDOG). To detect retinal vessels, the retinal image's response to the matched filter is thresholded using an adaptive threshold obtained from the image's response to the FDOG.

In this paper, we use a multi-scale technique to segment the vessels and extend our earlier conference results [14]. We introduce a medialness function (previously used to detect tubular structures in the 3D space [15]) for the 2D space and weight it with a function designed to reduce the effect of asymmetric structures. To improve the results for the vessel-like structures, the resulting image is multiplied by the smoothed eigenvalues of the Hessian matrix at every pixel of the image. Next, to eliminate noise from the image background while retaining vascular structures, we apply a noise reduction step that uses a formula based on area and elongation. A reconnection step is then applied for connecting truncated vessels based on structural characteristics of the retinal vessels. Finally, the exact boundaries of vessels are estimated using eigenvalues and the result of the medialness function. To evaluate the performance of our algorithm, we tested it on the DRIVE and STARE databases and compared our results with those reported in recent articles.

The rest of the paper is organized as follows. In Section 2, we detail the methods used for vessel segmentation. Experimental results are presented and compared with other methods in Section 3. Finally, we discuss our results and conclude in Section 4.

## 2. Proposed methods

Since the green channel of color retinal images provides the highest contrast between vessels and background in retinal image analysis [16], the green channel of these images is used as input to our vessel segmentation algorithm (Fig. 1). Fig. 2 shows a block diagram of our proposed scheme. The method has three major phases: vessel medialness detection; vessel centerline extraction; and vessel reconstruction. Each phase is subdivided into several steps as follows:

**Vessel medialness detection:** (1) *Multi-scale vessel medialness detection* is applied at several scales using a weighted medialness function to extract the medial line of vessels. (2) *The sum of eigenvalues* is used to strengthen the vessel medial response,



Fig. 1. Green channel of image 16 from DRIVE dataset.

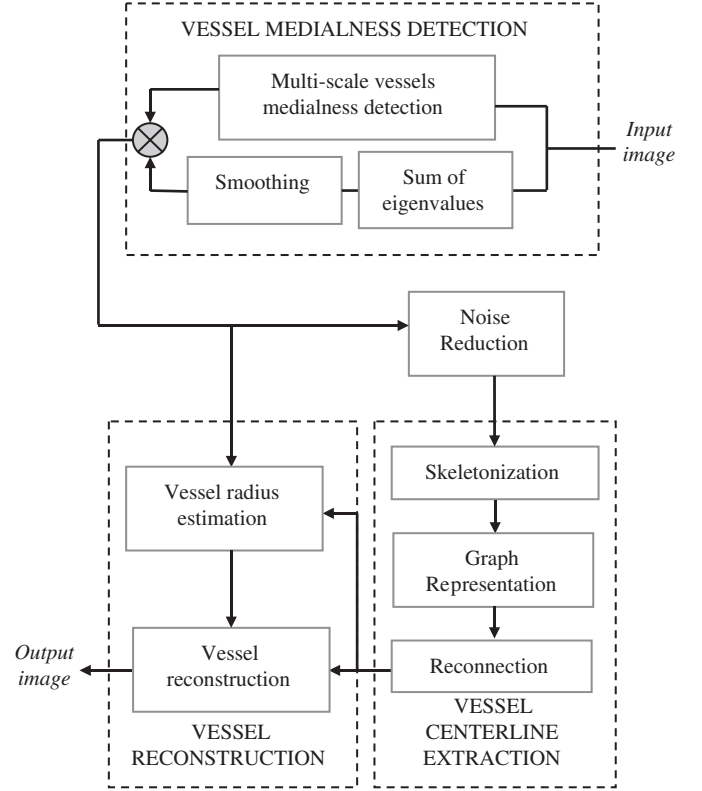


Fig. 2. A block diagram of the proposed method of vessel segmentation.

which has been attenuated due to an adaptive threshold in a previous step.

**Vessel centerline extraction:** (1) *Skeletonization* is applied to extract the skeleton of vessels. (2) *Graph representation* is obtained by labeling the pixels as an end-, curve-, or branch-point and finding the edge of the graph. (3) *Reconnection* is connecting disconnections in vessels tree based on the vessel's structural characteristics.

**Vessel reconstruction:** (1) *Vessel radius estimation* based on the information obtained from each step of phase 1, using eigenvalues and the result of the medialness function. (2) *Vessel reconstruction* using the estimated radius and the vessels' graph.

In addition, a noise-reduction step is used to suppress background noise and reduce the complexity of the other steps, especially the reconnection step. The details of these steps are explained in the next subsections.

### 2.1. The vessel medialness detection filter

Because of robustness of the medialness function in extracting tubular structures, this function has been previously applied for segmenting these structures in 3D space. The initial medialness function is defined in [17] as follows:

$$m_0(y, \sigma) = \int_{R^n} b(x, \sigma) \delta(y - x - r \hat{n}(x, \sigma)) d^n x \quad (1)$$

where  $\delta$  is the delta function. For each point  $x$  in the boundaryness space, the initial contribution  $b(x, \sigma) = |\mathbf{B}(x, \sigma)|$  is made at  $y = x + r \hat{n}(x, \sigma)$  where  $\hat{n}$  is a unit vector determined by  $\hat{n}(x, \sigma) = \mathbf{B}(x, \sigma) / |\mathbf{B}(x, \sigma)|$ ,  $r$  is a variable that changes according to scale  $\sigma$  as  $r = k\sigma$  (where  $k$  is constant),  $B(x, \sigma)$  is the boundaryness function and is equivalent to the image gradient at the point  $x$  in the image convolved with a Gaussian with standard deviation  $\sigma$ . The relationship of the medialness function to boundaryness is illustrated in Fig. 3.

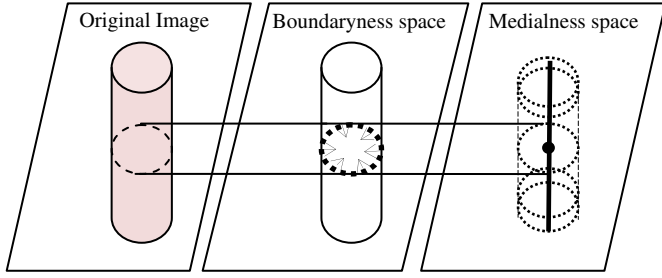


Fig. 3. A response of the medialness function obtained from the boundaryness measures.

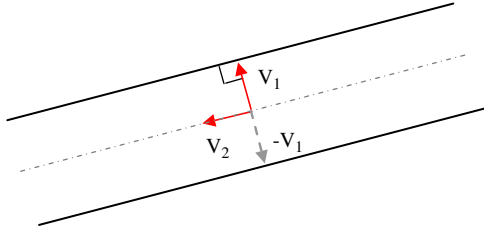


Fig. 4. Orientation of the eigenvectors of the Hessian matrix at the centerline of the vessel.

To reduce the influence of asymmetric structures and edges, the boundaryness function is weighted by the weighting function  $p(x, \sigma)$ , called the contribution confidence [17]:

$$p(x, \sigma) = 1 - \frac{b(x, \sigma)}{m_0(y, \sigma)} \quad (2)$$

hence, the weighted medialness is given by

$$m(y, \sigma) = \int_{R^n} b(x, \sigma) p(x, \sigma) \delta(y - x - r\hat{\mathbf{n}}(x, \sigma)) d^n x \quad (3)$$

Since in 2D space, there are two vectors perpendicular to the path of the vessel, we must consider two directions in our algorithm (Fig. 4). Therefore, we define a 2D version of multi-scale weighted medialness by modifying Eq. (3) as

$$m(\mathbf{x}, \sigma) = \frac{1}{2} \sum_{i=1}^2 b_i(\mathbf{x}, \sigma) p(b_i, \sigma) \quad (4)$$

here  $m$  is the weighted medialness function and its variables are the position of each pixel  $\mathbf{x}$  and the scale  $\sigma$ . Each  $b_i$  is a 2D function defined as follows:

$$b_1(\mathbf{x}, \sigma) = \nabla I^{(\sigma)}(\mathbf{x} + \theta \sigma \mathbf{v}_1) \quad b_2(\mathbf{x}, \sigma) = \nabla I^{(\sigma)}(\mathbf{x} - \theta \sigma \mathbf{v}_1) \quad (5)$$

where  $\nabla I^{(\sigma)}(\mathbf{x})$  is the gradient at the pixel  $\mathbf{x}$  in the image convolved with a Gaussian kernel with standard deviation of  $\sigma$ . In this equation,  $\theta$  is a constant coefficient that defines the relation of the vessels' radii and the scales at which they should be detected,  $\mathbf{v}_1$  is a vector perpendicular to the vessel's path at point  $\mathbf{x}$  and is the eigenvector corresponding the largest eigenvalue of the Hessian matrix. The Hessian matrix is obtained by calculating the second derivatives of the image intensity ( $I$ ):

$$\nabla^2 I(\mathbf{x}) = \mathbf{H}(\mathbf{x}) = \begin{bmatrix} I_{xx}(\mathbf{x}) & I_{xy}(\mathbf{x}) \\ I_{yx}(\mathbf{x}) & I_{yy}(\mathbf{x}) \end{bmatrix} \quad (6)$$

Moreover,  $p(b_i, \sigma)$  is the following exponential function:

$$p(b_i, \sigma) = \exp\left(-\left(1 - \frac{b_i}{(b_1 + b_2)/2}\right) / (2\sigma^2)\right) \quad (7)$$

Since retinal vessels are symmetric structures about their medial lines and the intensity of the vessel section can be modeled by a Gaussian function, choosing a weighting function

as shown in Eq. (7) emphasizes the vessel's structures and weakens other structures.

To reduce background noise, we use adaptive thresholding using the gradient  $\nabla I^{(\sigma)}$  according to

$$m_2(\mathbf{x}, \sigma) = \begin{cases} m(\mathbf{x}, \sigma) - \nabla I^{(\sigma)}(\mathbf{x}) & \text{if } m(\mathbf{x}, \sigma) > \nabla I^{(\sigma)}(\mathbf{x}) \\ 0 & \text{otherwise} \end{cases} \quad (8)$$

It can be shown that near the main axis of vessels,  $m$  is greater than  $\nabla I^{(\sigma)}$ . Therefore, after applying this function, the medial lines of vessels are enhanced. The result is then obtained by maximizing the response of the medialness function ( $m_2$ ) at different scales.

$$R_{multiscale} = \max_{scale} (m_2(x, \sigma)) \quad (9)$$

Although the adaptive thresholding shown in Eq. (8) attenuates the background noise, it also diminishes the response of the vessels' pixels. Therefore, using the eigenvalues of the Hessian matrix that have a strong response in the vessels can reduce this effect. In order to reduce the impact of image nonuniformity, we first convolve the sum of eigenvalues with a Gaussian kernel. Then, by multiplying the consequent image by the response of multi-scale medialness function, the vessels are properly enhanced. Therefore, the final vessel medialness detection filter is given by

$$R_{medial} = R_{multiscale} \times (\text{Gaussian} \otimes (\lambda_1 + \lambda_2)) \quad (10)$$

Fig. 5(a) illustrates the result of applying the vessel medialness detection filter on a retinal image. Note that this filter properly extracts line-like structures from the image. Fig. 5(b) is the result of simple thresholding of Fig. 5(a).

Since the radii of the retinal vessels change logarithmically based on their structural characteristics, the scales can be selected logarithmically in  $[a, b]$ , where  $a$  and  $b$  are chosen according to the maximum and minimum size of vessels in the retinal image. The number of scales affects the accuracy in estimating the size of the vessels, whereas the algorithm is slowed when more scales are used. The scales are therefore selected as follows:

$$Scale(i) = \exp\left(\log(a) + \frac{(i-1)(\log(b) - \log(a))}{(N_s - 1)}\right) \quad (11)$$

where  $N_s$  is the number of scales.

## 2.2. Noise reduction

Noting that the result of the previous phase is not noise-free, a noise reduction step to suppress noise and reduce the complexity of the following steps, especially the reconnection step, is imperative.

It is clear that noise structures are usually smaller than the vessels. Thus, a simple approach used in previous work [18–20] is applied to remove small connected components by morphological operations. However, this approach also removes fine vessels and capillaries. Therefore, a method that removes noise and preserves fine vessels and capillaries will be preferred. For this purpose, we consider three assumptions to discriminate noise from vessels:

1. The components with large areas can be supposed to be vessels whereas noisy pixels usually are small connected components.
2. Very small structures and single pixel components either located near the vessels or distributed in a definite direction can be assumed to be fine vessels and capillaries whereas noise has a sparse distribution.
3. The structures with high elongation belong to the vessels and the heap-like (not elongated) structures are assumed to be noise.

Based on these assumptions, we first connect small components that are close to each other and located in specific directions by the bridge morphological operation. Then, the structures

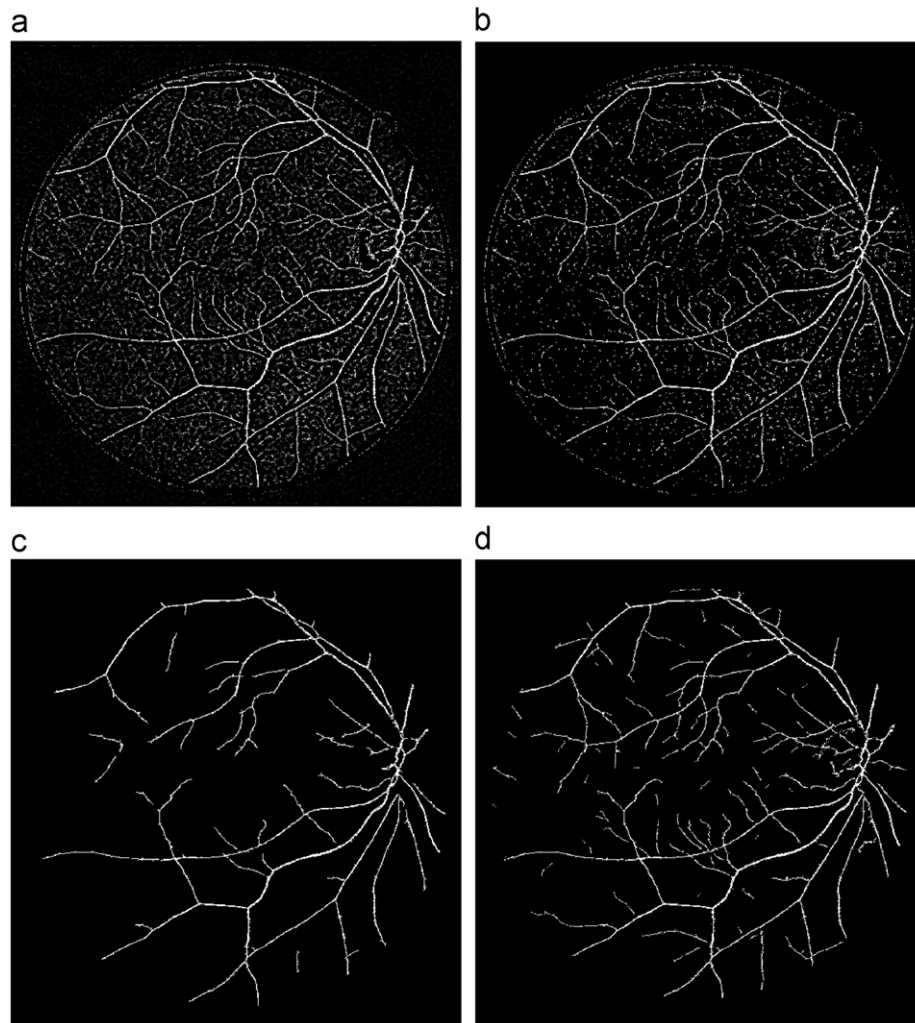


**Fig. 5.** (a) Detection of vessels of image in Fig. 1 by the vessel medialness detection filter. (b) Result of simple thresholding. (c), (d) Removing noise by the use of morphological operators and the proposed method with two parameters (area and elongation).

are classified as noise or vessels based on their area and elongation. If these parameters for a component are smaller than experimentally determined thresholds, the component is considered as noise and removed from the image.

Fig. 5(c) and (d) shows the results of two approaches for noise suppression. In Fig. 5(c), a simple morphological operation designed to remove small connected components is applied while in Fig. 5(d), the result of our proposed method is depicted.

### 2.3. Vessel centerline extraction

In spite of our attempt to keep vessels and suppress noise, a vascular network with some disjoint points is obtained after the noise reduction step. To connect these disjoint points, a reconnection step is proposed that works on one-pixel trees. As such, the skeleton of the vascular network is extracted first. Then, each pixel is labeled as a branch-, end-, or curve-point by the number of 8-adjacent pixels ( $n_8$ ) according to the following rule:

- $n_8 = 1$ : end-point
- $n_8 = 2$ : curve-point
- $n_8 \geq 3$ : branch-point

Since there are several separated connected components in the vascular network, each of them can be supposed to be a graph so

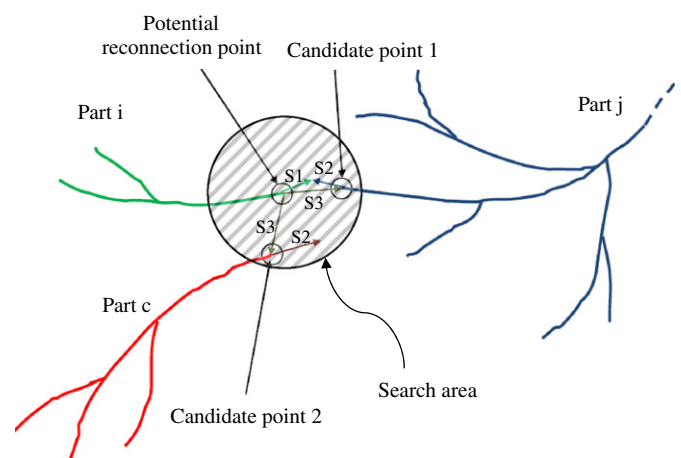


**Fig. 6.** Slope vectors used in the slope changing-constraint.

that the end-points and the branch-points are vertices of the graph and each edge of the graph is the curve-points located between the two vertices.

The reconnection algorithm is carried out between each two connected components (two graphs)  $p_i$  and  $p_j$  if the following topological restrictions are fulfilled (see Fig. 6).

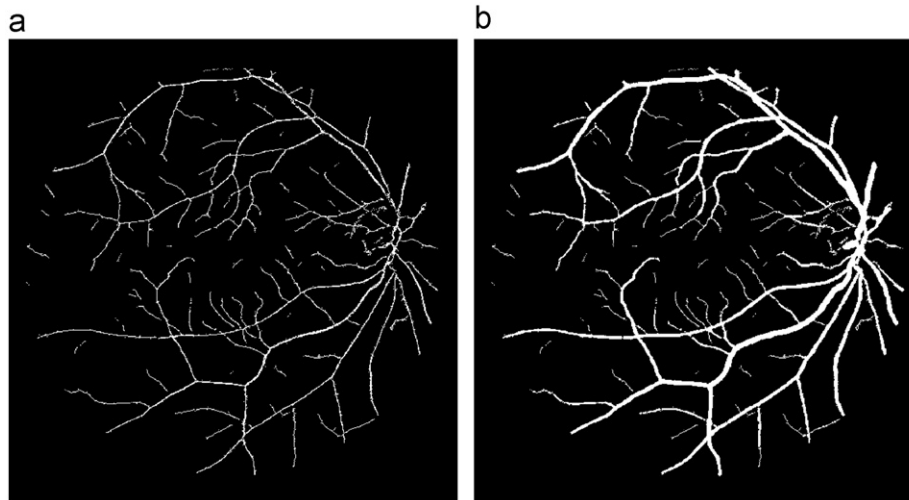


Fig. 7. (a) Vessels after reconnection with  $\theta_{\max} = 60^\circ$ ,  $\theta_{\min} = 120^\circ$ ,  $l_{\min} = 6$ , and  $l_{\max} = 13$ . (b) Final result of segmentation.

**Potential reconnection point:** Given the graph  $p_i$ , the potential reconnection point is defined by the end-point  $E_p$  of  $p_i$  that satisfies the following condition:

$$k = 1, \dots, L, k \neq P \quad R_v(E_p) > R_v(E_k) \quad (12)$$

here  $L$  is the number of end points in  $p_i$  and  $R_p$  is the radius of the vessel where each end-point is located. It indicates that the end-point located in the thickest vessel of the component is chosen as the potential reconnection point.

**Search area:** The reconnection path must lie around a potential reconnection point and inside a circular search area of radius  $r_s$ . In our reconnection algorithm, the radius of the search area is restricted by the following equation:

$$r_s = \begin{cases} l_{b_p} & \text{if } l_{\min} < l_{b_p} < l_{\max} \\ \max(l_{b_k}) & \text{if } l_{\min} < \max(l_{b_k}) < l_{\max} \& l_{b_p} < l_{\min} \\ l_{\min} & \text{if } \max(l_{b_k}) < l_{\min} \& l_{b_p} < l_{\min} \\ l_{\max} & \text{if } l_{b_p} > l_{\max} \end{cases} \quad (13)$$

here  $l_{\min}$  and  $l_{\max}$  are two constant numbers, the minimum and the maximum length of a reconnection path allowed in the algorithm. The  $l_{b_p}$  is the length of branch  $b_p$  on which the potential reconnection point is located and  $l_{b_k}$  is the length of any other branch,  $b_k, k = 1, \dots, L, k \neq P$  of the graph  $p_i$ .

**Candidate points:** The end-points of other graphs, i.e.  $p_j$ , located inside the search area of a potential reconnection point are called candidate points  $E_C$ .

**Radius constraint:** Since the vessel radius gradually decreases from the root of a vessel tree into its branches, the following condition should hold between the potential reconnection point and the candidate point:

$$R_v(E_p^{p_i}) \leq R_v(E_C^{p_j}) \quad (14)$$

where  $E_p^{p_i}$  is the potential reconnection point of graph  $p_i$  that should be connected to the candidate point  $E_C^{p_j}$  of graph  $p_j$ .  $R_v$  is the radius of the vessel where the potential reconnection point or the candidate point is located.

**Slope-changing constraint:** Based on structural characteristics of vessels, it is obvious that sharp changes of slope do not occur between two disjoint points of a vessel but an acute angle (sharp changes) may exist at the junctions. Therefore, a connection between two truncated parts of a vessel can be carried out when these two parts have similar slopes. Fig. 6 graphically demonstrates the connection of two disjoint points according to the slope-changing constraint.  $S_1$  and  $S_2$  are the vectors that show

slopes of the potential reconnection point and the candidate point, respectively; and  $S_3$  is the vector that connects the potential point to the candidate point. If angles,  $\theta_1$  and  $\theta_2$ , between the vectors comply with the following restrictions, these disjoint points are candidates for reconnection:

$$\begin{aligned} \theta_1 &= \cos^{-1}(\langle S_1, S_3 \rangle) < \theta_{\max} \\ \theta_2 &= \cos^{-1}(\langle S_1, S_2 \rangle) > \theta_{\min} \end{aligned} \quad (15)$$

where  $\langle \cdot, \cdot \rangle$  is inner product operation.

In summary, a connection between a potential point and a candidate point is performed if the radius and slope constraints are satisfied. The result of the reconnection algorithm is shown in Fig. 7(a).

#### 2.4. Radius estimation

To estimate the radii of the vessels, we use information derived from each step of phase 1. Since each vessel with a specific radius appears best at a particular scale of the medialness function, we can ascribe a unique radius ( $r_1 = \theta\sigma$ ) to each scale. The  $r_1$  describes the maximum symmetrical radius, which an object can have at a particular scale. On the other hand, the eigenvalues determine the edges of vessels that can be used for estimating the radii ( $r_2$ ) of vessels. By comparing  $r_1$  and  $r_2$ , we can discriminate vessels from abnormal regions and estimate an exact radius for a vessel. Since noise and abnormal regions are usually asymmetric structures, if  $r_2$  is much larger than  $r_1$ , this structure will be an abnormal region and no radius is estimated for this region; otherwise,  $r_1$  is selected as the vessel's radius. Using this estimation and the centerlines extracted from previous phase, the final result for segmentation of the retinal vessels is attained (Fig. 7(b)).

### 3. Experiments and results

#### 3.1. Databases

Our proposed method was tested on images from two publicly available databases DRIVE<sup>1</sup> and STARE<sup>2</sup>, collected by Niemeijer et al. [21] and Hoover et al. [3], respectively. The DRIVE database contains 40 color retinal images, with  $565 \times 584$  pixels and 8 bits

<sup>1</sup> Available at <http://www.isi.uu.nl/Research/Databases/DRIVE/>.

<sup>2</sup> Available at <http://www.parl.clemson.edu/stare/probing/>.

per color channel, in LZW compressed TIFF format. The images were originally captured by a Canon CR5 nonmydriatic 3 charge-coupled device (CCD) camera with a 45° field of view (FOV) and saved in JPEG format. In order to demarcate the FOV, a mask is provided for each image of this database. The database also consists of a set of binary images with the results of manual segmentation. These binary images have already been used as ground truth for evaluating the performance of several vessel segmentation methods [21]. The 40 images were divided into a training set and a test set by the authors of the database. The results of the manual segmentation are available for all the images of the two sets. For the images of the test set, a second independent manual segmentation also exists.

The second database, STARE, includes 20 images captured by a TopCon TRV-50 fundus camera with a 35° FOV and digitized to images of size of 650 × 550 with 8 bits per color channel. All images were manually segmented by two observers.

### 3.2. Parameter setting

The results reported in this paper have been obtained using the parameter values in Table 1. All of the parameters have been set based on an image randomly selected from the DRIVE dataset and used without any changes on the other images of the DRIVE and STARE datasets. In Table 2, the effect of the number of scales on the performance of our method in terms of accuracy for two images of the DRIVE dataset is shown. For both images, selecting seven scales seems to be the best choice. Therefore, this value has been used in all of our experiments. Also, since scales smaller than 0.4 or greater than 4 do not show significant parts of vessels, these seven scales were chosen using the logarithmic distance shown in Eq. (11) between 0.4 and 4.

In the noise reduction step, we have two parameters, area and elongation. To optimize these parameters, we first estimated the background noise using some of the images obtained after phase 1 and their ground truth images. We have experimentally found that most of noise structures have elongation and area smaller than 0.98 and 32, respectively. Selecting the value of these two parameters involved a trade-off between detection of thin vessels

and noise immunity. Due to the significant influence of the reconnection step on segmentation accuracy, this level should be controlled by reconnection parameters  $\theta_{\min}$ ,  $\theta_{\max}$ ,  $l_{\min}$ , and  $l_{\max}$ . We have determined the value of these parameters according to the structural characteristic of the retinal vessels.

### 3.3. Results

To evaluate our results and compare them with previous retinal vessel segmentation algorithms, segmentation accuracy has been chosen as one of the performance measures reported in this paper. The accuracy is estimated as the ratio of the total number of correctly detected pixels to the total number of pixels inside the image FOV. The ground proof for calculating the performance measures is the manual segmentation result. The fraction of pixels erroneously detected as vessel pixels (false positive ratio (FPR)) and the fraction of pixels correctly detected as vessel pixels (true positive fraction (TPR)) have also been reported. Furthermore, receiver operating characteristic (ROC) curves are used to compare our results with other retinal vessel segmentation methods. In an ROC curve, the true positive rate (TPR) versus false positive rate (FPR) is plotted. For an optimal system, this curve approaches the top left corner. Another performance measure, extracted from the ROC curve, is the area under the curve (AUC), which ideally equals 1.

To evaluate the effect of the adaptive thresholding, noise reduction, and reconnection steps on the performance of the proposed method, the TPR, FPR, and accuracy for each step has been calculated and reported in Table 3. In this table, the values of TPR and FPR demonstrate the effectiveness of each step of the proposed algorithm. As previously stated, adaptive thresholding attenuates the background noise and also weakens the response of the vessels' pixels. Therefore, TPR and FPR are noticeably increased when adaptive thresholding is not applied. Furthermore, the background noise is reduced during the noise reduction step, which is helpful in decreasing the FPR. However, it is likely that fine vessels are also eliminated during this process, leading to lower TPR. Thus, without the noise reduction step, these values should rise. Although TPR is improved by connecting the truncated vessels using the reconnection step, it is important to note that joining two disjoint points by a straight line cannot be a faultless method. Therefore, the reconnection step improves the TPR while worsening the FPR slightly. Consequently, each of these steps plays an important role in improving the vessel segmentation results.

To compare our results with those of several recent methods, the ROC curves of the DRIVE and STARE databases are shown in Fig. 8(a) and (b), respectively. Observing the sharp slopes of both ROC curves of our method in these figures, we can infer that our algorithm can reach high TPR while keeping FPR low.

As an alternative assessment, the performance measures of the methods, including ours, are compared in Tables 4 and 5. In Table 4, the average and standard deviation of accuracy, TPR, FPR, and area under the ROC curve for the 20 images of the DRIVE test set are reported. The same measures for 20 images of the STARE

**Table 1**  
Values of parameters used in the experiments.

Parameter	Value
Number of scales	7
Minimum of scales ( <i>a</i> )	0.4
Maximum of scales ( <i>b</i> )	4
Area	32
Elongation	0.98
$\theta_{\min}$	60
$\theta_{\max}$	120
$l_{\min}$	6
$l_{\max}$	13

**Table 2**  
Comparison of accuracy in terms of number of scales.

Number of scales	Accuracy % (Image 19 of DRIVE dataset)	Accuracy % (Image 6 of DRIVE dataset)
4	97.29	95.52
5	97.56	95.71
6	97.59	95.80
7	97.67	95.87
8	97.60	95.85

**Table 3**  
Effect of each step on performance of the algorithm.

	TPR	FPR	Accuracy
With noise reduction and reconnection	0.8401	0.0037	0.9767
Without adaptive thresholding	0.9328	0.0722	0.9284
Without noise reduction	0.8710	0.0241	0.9627
Without reconnection	0.7863	0.0032	0.9704

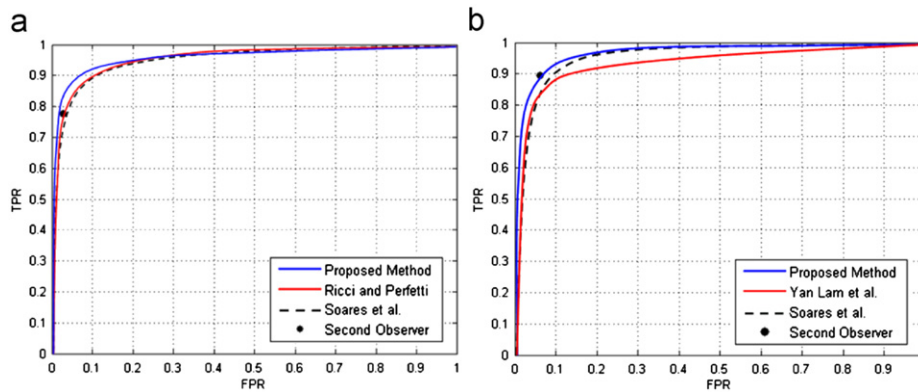


Fig. 8. ROC curves for the (a) DRIVE and (b) STARE databases for three different methods.

**Table 4**  
Performance of vessel segmentation methods on drive images.

Method	Average accuracy (standard deviation)	True positive rate	False positive rate	Area under ROC
2nd-observer	0.9473 (0.0048)	0.7761	0.0275	N/A
Multi-scale	0.9659 (0.0047)	0.7852	0.0065	0.9580
Ricci and Perfetti [8]	0.9595 (N/A)	N/A	N/A	0.9633
Soares et al. [6]	0.9466 (N/A)	N/A	N/A	0.9614
Mendonça and Campilho [11]	0.9463 (0.0065)	0.7315	0.0219	N/A
Staal et al. [23]	0.9442 (0.0065)	0.7194	0.0227	0.9520
Marín et al. [10]	0.9452 (N/A)	N/A	N/A	0.9588
Lupaşcu et al. [9]	0.9597(0.0054)	0.6728	0.0126	0.9561
Vlachos and Dermatas [5]	0.9285(0.0088)	0.7468	0.045	N/A
Zhang et al. [13]	0.9382 (N/A)	0.7120	0.0276	N/A

**Table 5**  
Performance of vessel segmentation methods on stare images.

Method	Average accuracy (standard deviation)	True positive rate	False positive rate	Area under ROC
2nd-observer	0.9354 (0.0171)	0.8949	0.0610	N/A
Multi-scale	0.9756 (0.0095)	0.8133	0.0091	0.9678
Ricci and Perfetti [8]	0.9646 (N/A)	N/A	N/A	0.9680
Soares et al. [6]	0.9480 (N/A)	N/A	N/A	0.9671
Mendonça and Campilho [11]	0.9479 (0.0065)	0.7123	0.0242	N/A
Staal et al. [23]	0.9516 (N/A)	0.697	0.019	0.9614
Hoover et al. [3]	0.9267 (0.0099)	0.6751	0.0433	0.9275
Yan Lam and Yan [12]	0.9474(N/A)	N/A	N/A	0.9392
Marín et al. [10]	0.9526 (N/A)	N/A	N/A	0.9769
Zhang et al. [13]	0.9484 (N/A)	0.7177	0.0247	N/A

dataset are represented in Table 5. These tables show that the average accuracy of the multi-scale method is superior to those of the other methods. These accuracy measures are due to a high value of TPR along with a low value of FPR. Another point for discussion regarding the results shown in these tables is that the area under ROC is also comparable to other methods, especially in the STARE dataset, which includes more pathological regions.

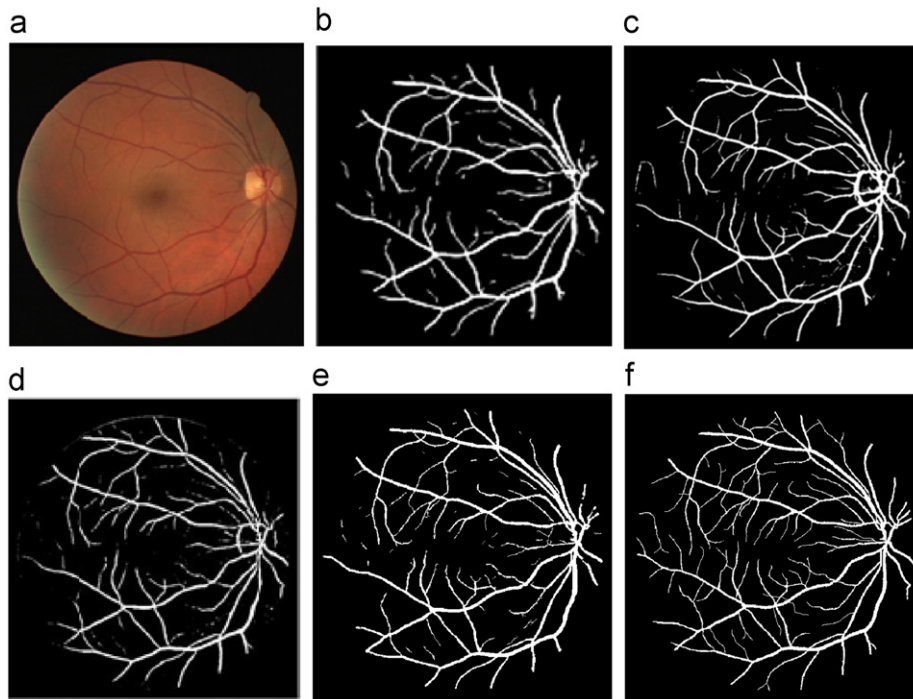
To prove our claims graphically, the result of the proposed method versus the results of Marín et al. [10], Lupaşcu et al. [9], and Ricci and Perfetti [8] on an image of the DRIVE dataset is shown in Fig. 9. It is obvious that the circle around the blind spot has properly been removed using our method and the method proposed by Marín et al. [10].

In Fig. 10, the effectiveness of the multi-scale retinal vessel segmentation method for eliminating heap-like structures compared with the methods of Mendonça Camphilo [11], Soares et al. [6], and

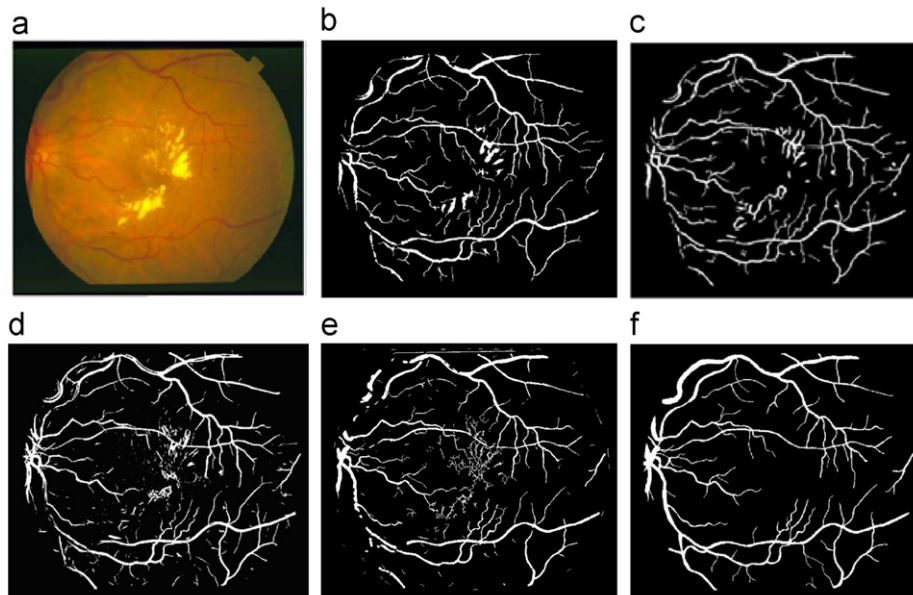
Zhang et al. [13] is illustrated. In this figure, the abnormal regions are far from the vessel areas. It is apparent that the multi-scale method has more successfully eliminated these heap-like structures from the background while appropriately detecting vessels.

Fig. 11 is another example from the STARE database with some abnormal regions in the vessel areas. In this situation, the multi-scale method has appropriately found vessels in the middle of abnormal regions. Although some vessels are truncated in these regions, the reconnection step has revived some connections of the vessels. Notice that this method achieved improved result (accuracy=0.9780) compared to the results of Soares et al. [6] and Yam Lam and Yan [12] (accuracy=0.9325 and 0.9140, respectively).

Finally, we show the worst and the best vessel segmentation results of the multi-scale retinal vessel segmentation method for the DRIVE and STARE datasets. Figs. 12 and 13 demonstrate the vessel centerlines, final vessel segmentation, and ground truth images.



**Fig. 9.** Sample results for the images of the DRIVE database. (a) The original image, (b) Marín et al. [10], (c) Ricci et al. [8], (d) Lupașcu et al. [9], (e) the proposed method, and (f) the ground truth.



**Fig. 10.** Sample results for the images of the STARE dataset with some abnormal regions. (a) The original image, (b) Mendonça and Campilho [11], (c) Zhang et al. [13], (d) Soares et al. [6], (e) our proposed method, and (f) the ground truth.

#### 4. Discussion and conclusion

In this paper, a new approach based on a multi-scale method for segmentation of retinal vessels was proposed. Using a medialness function in the form of a 2D multi-scale function assisted us in detecting the medial lines of the vessel structures. Also, combining the results of the eigenvalues of the Hessian matrix and the medialness function, the vessels were further enhanced. Although the Hessian matrix has strong response in the vessels, it does not have large eigenvalues at the crossings and bifurcations and thus Hessian-based methods have problems at these points. On the other hand, the medialness function generates acceptable results at these

points. Therefore, it can be concluded that the medialness function and the eigenvalues of the Hessian matrix are complementary and their combination can enhance medial lines of the vessel structures in comparison with either of them alone [22].

In the result section, we showed that the FPR for the proposed method is remarkably low in comparison with the other methods since it has the ability to avoid the blind spot area and abnormal regions. In fact, this is due to the inherent property of the medialness function, which detects symmetric structures, and also the noise reduction step, which decreases the FPR by removing noise. Consequently, we can claim that our method is capable of having superior performance in pathological retinal images.

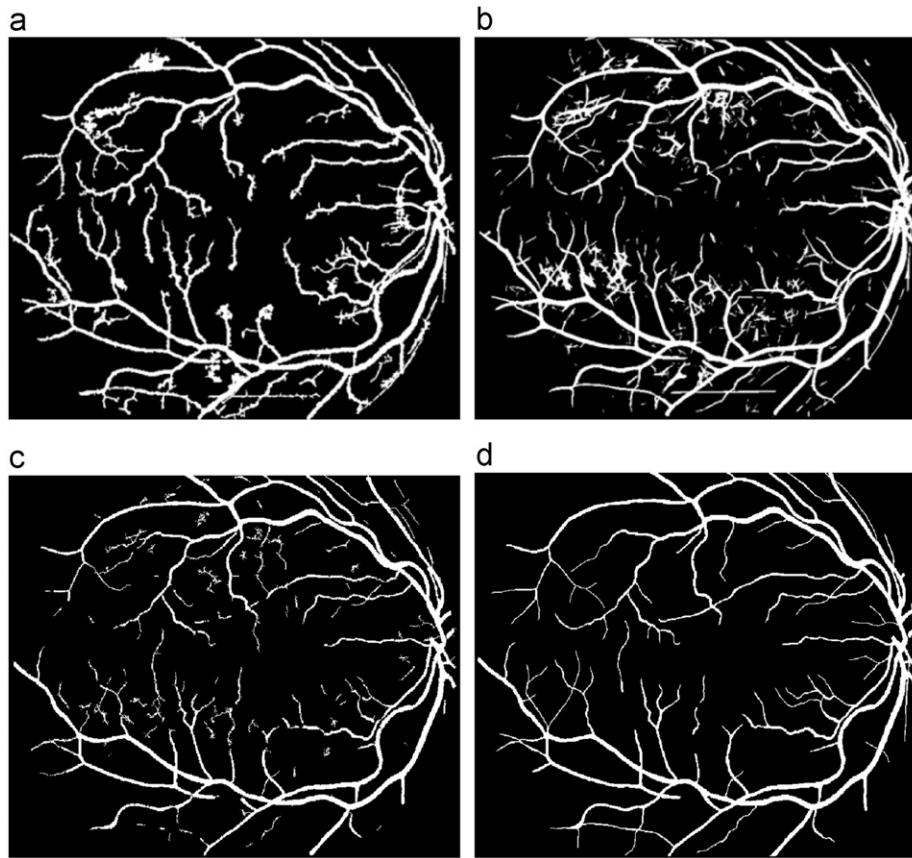


**Fig. 11.** Results for an image of the STARE dataset with abnormal regions. (a) Yan Lam and Yan [12] (TPR; FPR)=(0.8935; 0.0839), (b) Soares et al. [6] (TPR; FPR)=(0.8981; 0.0640), (c) the proposed method, (TPR; FPR)=(0.8686; 0.0108), (d) ground truth.

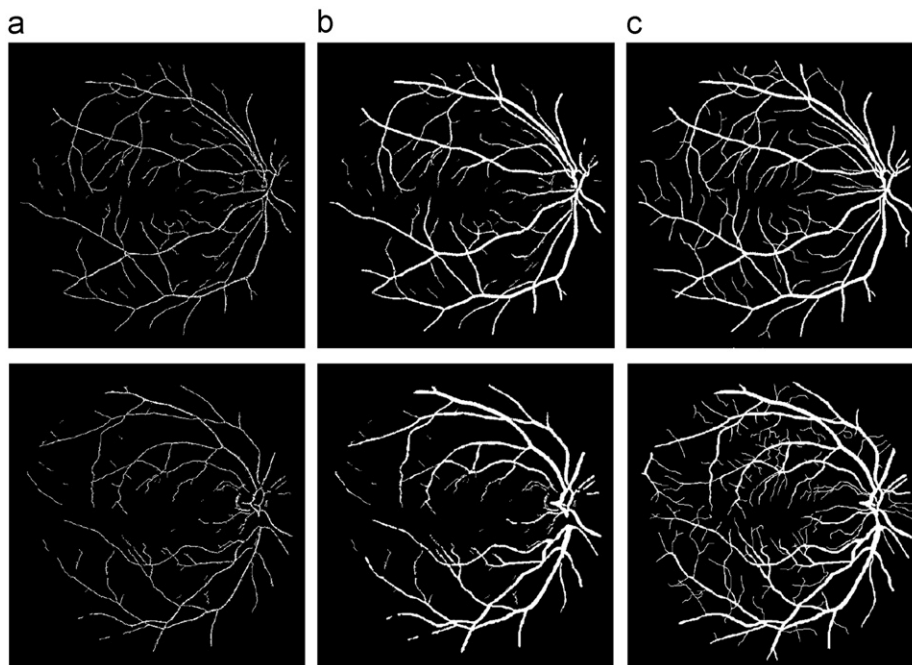


**Fig. 12.** First row: best result of the DRIVE dataset (accuracy=0.9759), second row: worst result of the DRIVE dataset (accuracy=0.9580). (a) Vessel centerlines, (b) final vessel segmentation, (c) ground truth.

Another advantage of the proposed method in comparison with classifier-based methods is that it does not require training data for segmenting the vessels. As explained in the

parameter setting section, the initial parameters can be set with only one image. Therefore, it is not obligatory to change these parameters when a new dataset is introduced to the system

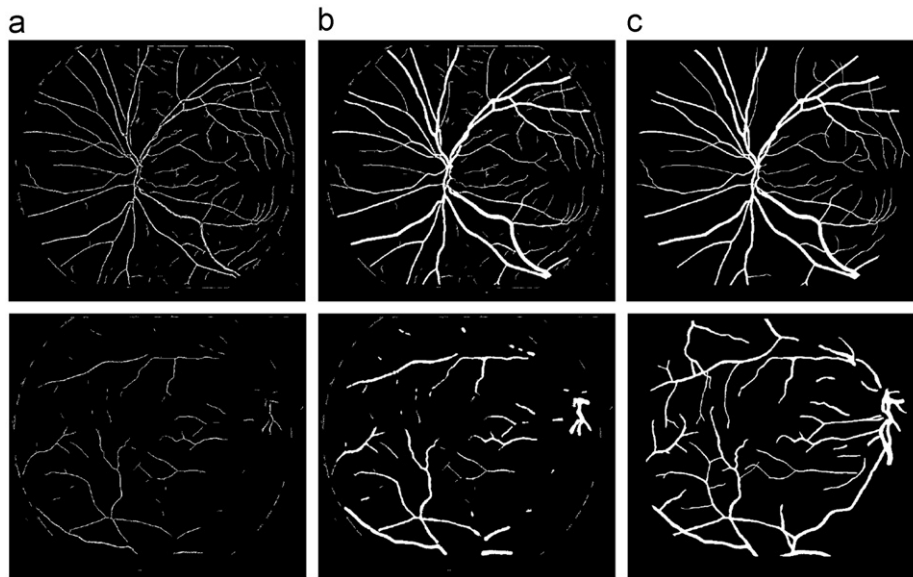


**Fig. 13.** First row: best result of the STARE dataset (accuracy=0.9865), second row: worst result of the STARE dataset (accuracy=0.9577). (a) Vessel centerlines, (b) final vessel segmentation, and (c) ground truth.

unless the general properties of the dataset are completely different.

Although our method has the above advantages, it may not detect fine vessels as well as some recent methods. For example, the TPR for our method is slightly different from the TPR of Soares et al. [6] and Yan Lam and Yan [12] as Fig. 11 shows. This is because some of the fine vessels are removed by the noise reduction step and these vessels are not revived by the reconnection step. This can be considered as a weakness of our algorithm. This event is aggravated when capillaceous vessels are located in an abnormal region, especially in a dark abnormal region. In this situation, only some isolated points may be detected, which are easily removed during noise reduction step, due to their shapes and being remote from the detected vessels. Hence, the two disjoint parts of vessels will be too separated to be reconnected in the reconnection step.

To address the above problem, we may merge the noise reduction and reconnection steps so that these steps operate simultaneously and the decision about removing a region or connecting it to another region is made concurrently. We expect that this would increase the intricacy and thus processing time of the algorithm. Another possible solution is to find the approximate location of the abnormal area and keep truncated vessels in this area by localizing the noise reduction step and adaptively setting the area and elongation parameters. This may lead to a more reliable input to the reconnection step.

## 5. Summary

Automatic segmentation of retinal vessels in optic fundus images has been of particular interest in recent years. Vessel segmentation is a prelude to the diagnosis of many retinal diseases and thus many articles have focused on proposing an efficacious method to address this problem. In this paper, we propose a multi-scale method to segment retinal vessels in 2D images based on a medialness function that was previously applied to the segmentation of tubular structures in 3D. To this end, the medialness function is multiplied by a weighting function, called the contribution confidence, to reduce the effect of asymmetric structures. Furthermore, to enhance the vessels, the results of the medialness function are multiplied by the eigenvalues of the Hessian matrix. Next, a noise reduction step is

applied to omit noise from the background of the image. For this purpose, the structures in an image are classified as noise or vessels based on their area and elongation. If parameters for a component are smaller than pre-defined thresholds, the component is considered as noise and removed from the image. In spite of attempting to keep fine vessels in the noise reduction step, some fine vessels may be removed along with the noise. Therefore, a reconnection step is applied to connect truncated vessels based on structural characteristics of the retinal vessels. Finally, the radii of the vessels are estimated using information from the first step. Since each vessel with a specific radius appears best at a particular scale of the medialness function, we ascribe a unique radius  $r_1$  to each scale, which describes maximum radius of an object in that scale. On the other hand, the eigenvalues determine edges of vessels that can be used to estimate radii ( $r_2$ ) of the vessels in the image. By comparing  $r_1$  and  $r_2$ , we discriminate vessels from abnormal regions and determine an exact radius for a vessel. Our proposed method is tested on images of two publicly available databases, DRIVE and STARE. The results show that the proposed algorithm can reach a high true positive ratio (TPR) while keeping the false positive ratio (FPR) low. They also illustrate that the average accuracy of the proposed multi-scale method for both databases is superior to those of several other methods in the literature. The area under the receiver operator characteristic (ROC) curve of the proposed method is comparable with those of the other methods. One of the main features of the proposed method is to avoid false vessel detection due to noise and pathological abnormality. Consequently, superiority of the method is more pronounced when using datasets with many pathological regions like the STARE dataset.

## Conflict of interest statement

The authors have no actual or potential conflict of interest including any financial, personal, or other relationships with other people or organizations to disclose.

## Acknowledgment

The authors thank Prof. Richard Hartley from Australian National University for his reading of the manuscript and

providing constructive suggestions. They also thank anonymous reviewers whose comments and suggestions improved presentation of the paper.

## References

- [1] J. Kanski, *Clinical Ophthalmology: A Systematic Approach*, Butterworth-Heinemann, London, U.K, 1989.
- [2] M.E. Martinez-Perez, A.D. Hughes, A.V. Stanton, S.A. Thom, N. Chapman, A.A. Bharath, K.H. Parker, Retinal vascular tree morphology: a semi-automatic quantification, *IEEE Trans. Biomed. Eng.* 49 (8) (2002) 912–917.
- [3] A. Hoover, V. Kouznetsova, M. Goldbaum, Locating blood vessels in retinal images by piecewise threshold probing of a matched filter response, *IEEE Trans. Med. Imag.* 19 (3) (2000) 203–210.
- [4] B. Al-Diri, A. Hunter, D. Steel, An active contour model for segmenting and measuring retinal vessels, *IEEE Trans. Med. Imag.* 28 (9) (2009) 1488–1497.
- [5] M. Vlachos, E. Dermatas, Multi-scale retinal vessel segmentation using line tracking, *Comput. Med. Imag. Graph.* 34 (2010) 213–227.
- [6] J.V.B. Soares, J.J.G. Leandro, R.M. Cesar Jr., H.F. Jelinek, M.J. Cree, Retinal vessel segmentation using the 2D Gabor wavelet and supervised classification, *IEEE Trans. Med. Imag.* 25 (9) (2006) 1214–1222.
- [7] M.E. Martinez-Prez, A.D. Hughes, S.A. Thom, A.A. Bharath, K.H. Parker, Segmentation of blood vessels from red-free and fluorescein retinal images, *Med. Image Anal.* 11 (2007) 47–61.
- [8] E. Ricci, R. Perfetti, Retinal blood vessel segmentation using line operators and support vector classification, *IEEE Trans. Med. Imag.* 26 (10) (2007) 1357–1365.
- [9] C.A. Lupaşcu, D. Tegolo, E. Trucco, FABC: retinal vessel segmentation using AdaBoost, *IEEE Trans. Inf. Technol. Biomed.* 14 (5) (2010) 1267–1274.
- [10] D. Marín, A. Aquino, M.E. Gegúndez-Arias, J.M. Bravo, A new supervised method for blood vessel segmentation in retinal images by using gray-level and moment invariants-based features, *IEEE Trans. Med. Imag.* 30 (1) (2011) 146–158.
- [11] A.M. Mendonça, A. Campilho, Segmentation of retinal blood vessels by combining the detection of centerlines and morphological reconstruction, *IEEE Trans. Med. Imag.* 25 (9) (2006) 1200–1213.
- [12] B.S. Yan Lam, H. Yan, A novel vessel segmentation algorithm for pathological retina images based on the divergence of vector fields, *IEEE Trans. Med. Imag.* 27 (2) (2008) 237–246.
- [13] B. Zhang, L. Zhang, L. Zhang, F. Karray, Retinal vessel extraction by matched filter with first-order derivative of Gaussian, *Comput. Biol. Med.* 40 (2010) 438–445.
- [14] E. Moghimirad, S.H. Rezaatofghi, H. Soltanian-Zadeh, Multi-scale approach for retinal vessel segmentation using medialness function, in: *Proceedings of the IEEE International Symposium on Bio-Medical Imaging*, 2010, pp. 29–32.
- [15] T.G. Pock, *Robust Segmentation of Tubular Structures in 3D Volume Data*, Master Thesis, University of Graz, 2004.
- [16] P. Feng, Y. Pan, B. Wei, W. Jin, D. Mi, Enhancing retinal image by the contourlet transform, *Pattern Recognition Lett.* 28 (2007) 516–522.
- [17] M. Xu, D. Pycocock, A scale-space medialness transform based on boundary concordance voting, *J. Math. Imag. Vision* 11 (3) (1999) 277–299.
- [18] T. Chanwimaluang, F. Guoliang, An efficient blood vessel detection algorithm for retinal images using local entropy thresholding, in: *Proceedings of the 2003 International Symposium on Circuits Systems*, 2003, pp. 21–24.
- [19] M. Sofka, C.V. Stewart, Retinal vessel centerline extraction using multiscale matched filters, confidence and edge measures, *IEEE Trans. Med. Imag.* 25 (12) (2006) 1531–1546.
- [20] Ch. Wu, J.J.K. Derwent, P. Stanchev, Retinal vessel radius estimation and a vessel center line segmentation method based on ridge descriptors, *J. Sign. Process. Syst.* 55 (1–3) (2009) 91–102.
- [21] M. Niemeijer, J. Staal, B. Van Ginneken, M. Loog, M.D. Abramoff, Comparative study of retinal vessel segmentation methods on a new publicly available database, in: *SPIE Med. Imag.*, J.M. Fitzpatrick and M. Sonka (Eds.) 5370 (2004) 648–656.
- [22] A. Frangi, W.J. Niessen, R.M. Hoogeveen, T. Walsum, M.A. Viergever, Model-based quantitation of 3-D magnetic resonance angiographic images, *IEEE Trans. Med. Imag.* 18 (10) (1999) 946–956.
- [23] J. Staal, M.D. Abramoff, M. Niemeijer, M.A. Viergever, B. van Ginneken, Ridge-based vessel segmentation in color images of the retina, *IEEE Trans. Med. Imag.* 23 (4) (2004) 501–509.